Exciton Fine Structure of CsPbCl 3 Nanocrystals: An Interplay of Electron–Hole Exchange Interaction, Crystal Structure, Shape Anisotropy, and Dielectric Mismatch

Victor Guilloux, Amal Ghribi, Silbé Majrab, Florent Margaillan, Mathieu Bernard, Frédérick Bernardot, Laurent Legrand, Emmanuel Lhuillier, Kaïs Boujdaria, Maria Chamarro, et al.

Exciton fine structure of $CsPbCl_3$ nanocrystals: an interplay of electron-hole exchange interaction, crystal structure, shape anisotropy and dielectric mismatch.

Victor Guilloux[§ Ł], Amal Ghribi[¶ Ł], Silbé Majrab[§], Florent Margaillan[§], Mathieu Bernard[§], Frédérick Bernardot[§], Laurent Legrand[§], Emmanuel Lhuillier[§], Kaïs Boujdaria[¶], Maria Chamarro[§], Christophe Testelin[§], and Thierry Barisien[§]*

[§] Institut des NanoSciences de Paris, CNRS UMR 7588, Sorbonne Université, F-75005 Paris, France

[¶] LR01ES15 Laboratoire de Physique des Matériaux : Structure et Propriétés, Faculté des Sciences de Bizerte, Université de Carthage, Bizerte 7021, Tunisia

[*] Correspondence: thierry.barisien@insp.jussieu.fr

KEYWORDS: exciton, exciton fine structure, perovskite nanocrystals, shape anisotropy, micro-photoluminescence, exchange interaction, dielectric confinement

ABSTRACT: In the semiconducting perovskite materials family, the caesium-lead-chloride compound ($CsPbCl_3$) supports robust excitons characterized by a blue-shifted transition and the largest binding energy, thus presenting a high potential to achieve demanding solid-state room temperature photonic or quantum devices. Here we study the fundamental emission properties of cubic-shape colloidal $CsPbCl_3$ nanocrystals (NCs), examining in particular individual NC responses - using micro-photoluminescence - in order to unveil the exciton-fine structure (EFS) features. Within this work, NCs with average dimensions $< L_\alpha > \approx 8$ nm ($\alpha = x, y, z$) are studied with a level of dispersity in their dimensions that allows to disentangle the effects of size and shape anisotropy in the analysis. We find that most of the NCs exhibit an optical response under the form of a doublet with crossed polarized peaks and an average inter-bright state splitting, $\Delta_{BB} \approx 1.53$ meV, but triplets are also observed though being a minority. The origin of the EFS patterns is discussed in the frame of the electron-hole exchange model by taking into account the dielectric mismatch at the NC interface. The different features (large dispersity in the Δ_{BB} values and occasional occurrence of triplets) are reconciled by incorporating a moderate degree of shape anisotropy - observed in the structural characterization - by preserving the relatively high degree of the NC lattice symmetry. The energy distance between the optically inactive state and the bright manifold, Δ_{BD}, is also extracted from time-resolved photoluminescence measurements ($\Delta_{BD} \approx 10.7$ meV) in good agreement with our theoretical predictions.

In previous years, organic and inorganic lead halide perovskites have come to the light as a new generation of promising semiconductor materials for low-cost solar cells,[1-3] or for a large variety of optoelectronic technologies such as light-emitting diodes,[4-6] lasers,[5,7,8] photo-detectors[9-11] as well as for more advanced applications in the spintronic domain.[12-15] Among these materials $CsPbCl_3$ has a particular status since it has the largest energy band gap associated to an absorption threshold and photoluminescence shifted in the blue spectral region.[16,17]

The synthesis of $CsPbCl_3$ nanocrystals (NCs)[18] and their doping with transition metals[19,20] or lanthanides[21] have been successfully achieved at the same time. Thus, the electronic properties of $CsPbCl_3$ NCs can be tuned by quantum confinement effects or modified and improved by doping. For example, the substitution of Pb^{2+} ions by Mn^{2+} ions leads to a new emission band in the red spectral region; it moreover modifies the magnetic properties of $CsPbCl_3$[22] and plays an important role in improving the efficiency and the stability of photovoltaic devices by converting the absorbed UV light into red-visible light.[23] It has also been demonstrated that rare earth ions doping of NCs could expand the emission capabilities: implementation of electroluminescent white light emitting devices[24] could be achieved thanks to Sm^{3+} doping whereas near infrared emission was obtained by incorporation of Yb^{3+} ions.[22,25]

Excitons are at the center of all the optical and electronic properties of $CsPbCl_3$ NCs. Because the Coulomb interaction between the electron and hole carriers is stronger in $CsPbCl_3$ than in other lead halide perovskites, the exciton state is characterized by a very small Bohr radius, a_X = 1.72 nm, and the exciton binding energy is comparable to the one of semiconductor materials like ZnO or AlN and larger than in other lead halide perovskites and more studied CdSe, CdTe or GaAs materials.[16] This robust exciton has allowed the observation of polaritonic effects at room temperature while in other more conventional semiconductors cryogenic conditions are required.[26]

In semiconductors, the electron-hole exchange interaction (e-h EI) related to the Coulomb interaction is responsible for the splitting of the lowest-energy degenerate exciton states leading to the called exciton fine structure (EFS).[27-29] The knowledge of the EFS is a crucial point with regard to the in-depth understanding and prediction of the material optical properties and resultant applications. In perovskite materials (bulk and NCs), the lowest energy e-h pairs are characterized by the total angular momentum J_e = 1/2 and J_h = 1/2 and bound by the Coulomb interaction.[30,31] In bulky materials, theories favoring the e-h EI as the driving interaction have defined a unified framework in which the EFS is directly related to the symmetry the crystalline lattice may adopt.

In absence of shape anisotropy and for crystals of cubic structure (O_h point group), the e-h EI splits the four lowest-energy degenerate exciton states in two groups of states: a threefold degenerate optically active (bright) state at higher energy with J_{ex} = 1 and an optically inactive (dark) singlet state (with J_{ex} = 0) placed at lower energy. As the lattice symmetry is lowered towards tetragonal (D_{4h} point group) or orthorhombic (D_{2h} point group) phases, the bright state manifold splits in energy as a consequence of the interplay between the e-h EI and the anisotropic crystal field. This lifting of degeneracy has been clearly evidenced in bulk crystals.[32] In NCs the e-h EI is enhanced by confinement effects as already demonstrated in several colloidal NCs with wurtzite or zinc-blende structure.[33-37] Moreover, the EFS description is complexified by two parameters (both impacting the e-h EI), that are the dielectric confinement – the dielectric mismatch between the inside and the outside of the NC strongly enhances interactions with coulombic origins[38-42] – and coulombic effects induced by the NC shape anisotropy.

Experimentally, the use of highly-resolved spectroscopic techniques has been applied to the study of the low-temperature photoluminescence (PL) of perovskite NCs ensembles and has revealed the spectral signatures of single NCs bright states in quite a few compounds like $FAPbI_3$,[43] $FAPbBr_3$,[44,45] $MAPbI_3$,[46] $MAPbBr_3$,[47] $CsPbI_3$,[48,49] the 'most studied' $CsPbBr_3$,[50-53] or materials with alloyed composition like $CsPb(BrCl)_3$.[54,55] If early studies in fully inorganic perovskites have

postulated an inversion in the bright state-dark state organization to explain the high emission efficiencies,[55] the hypothesis is now reconsidered for the Rashba effect initially suspected to be at the origin of the inversion cannot be dominant in confined NCs.[56] Moreover, in hybrid compounds like $FAPbBr_3$ [45] and $CsPbI_3$,[49] the lowest energy state in the EFS was unambiguously identified as a dark state by resorting to a magnetic field to enhance the dark state optical activity (and make it detectable) through its coupling to the bright manifold. In this context, the fine structure of $CsPbCl_3$ remained until now unexplored while the strong Coulomb interaction present in this material shall allow to observe the largest excitonic splittings confirming the main role of the e-h EI in halide perovskite NCs EFS.

In this work we conduct a comprehensive study of the PL properties associated to $CsPbCl_3$ NCs in dense phases (ensembles) or as individual emitters. Our measurements, that clearly allow to characterize single NC emission patterns, indicate that the EFS bright state splitting amplitudes are indeed among the largest among halide perovskite NCs of comparable mean size over Bohr exciton diameter ratio, $L/2a_X$. The experimental results are thoroughly correlated to the output of EFS calculations based on the e–h EI and crystal field model in crystals of tetragonal symmetry (D_{4h} point group), taking explicitly into account the large dielectric mismatch at the NCs interface as well as the actual NC cuboid shape. The low degree of size dispersity (with a central size that dominates the population distribution) allows to consider shape anisotropy as an independent significant parameter in the analysis. As a refinement of the model, shape anisotropy is thus considered (applying NCs deformations in the simulations) and is shown to account for the large dispersity in the splitting values (that would not be explainable through size modulation of isotropic NCs exclusively). In order to draw an improved picture of the EFS in the chloride representative, time resolved PL experiments are also carried out. Their analysis is done classically in the frame of a back-transfer population model from the EFS dark state which localization in energy is extracted and found as is predicted by the theory. Finally, we sum up within a short review encompassing single NCs PL results obtained until now in halide perovskites and we discuss them in the framework of the e-h EI model.

RESULTS AND DISCUSSION

TEM Images Analysis and Steady-State Optical Spectroscopy. Before discussing the optical response of NCs in ensembles (deposited films) and to be able to correlate the structural parameters and the EFS signatures in the optical spectra (in particular gain insights on the role of shape anisotropy), a size analysis is performed from an exhaustive inspection of the TEM images (a typical snapshot is provided in Figure 1a). By discriminating the two 'in-plane' accessible dimensions, a 2D size-distribution histogram is built and provides a clear access to the manner NCs geometries depart from an ideal cubic structure. Figure 1b shows that the most occupied classes are for lateral dimensions L_1 and L_2 ($L_1 \geq L_2$) being of the same order i.e. $\langle L \rangle \approx 8.0 \pm 0.5$ nm, indicating that most of the addressed NCs are of cubic or nearly-cubic shape (we note that the 2D organization does not allow to distinguish a third independent direction). The population of classes outside the bisector borderline clearly reveals that a significant shape anisotropy is present among the NCs population that, at the macroscopic scale, will contribute to the broadening of the absorption and PL signals.

The reduced histogram of the L_1/L_2 parameter (inset of Figure 1b) provides a rough but relevant estimation of the average NCs distortion amplitude (Noting σ_{anis} the full width at half maximum – FWHM thereafter - we find here $\sigma_{anis} \approx 1.2 \pm 0.05$). The micro-PL results presented in the following sections will be discussed, in part, with regard to this characteristic value. It is important noticing that L_1 and L_2 are not specified with respect to the dimension they refer to, as a

consequence the anisotropy factor that should be considered to match the experimental characterization is actually in the σ_{anis}^{-1} - σ_{anis} range (ie the ≈ 0.8 - 1.2 range).

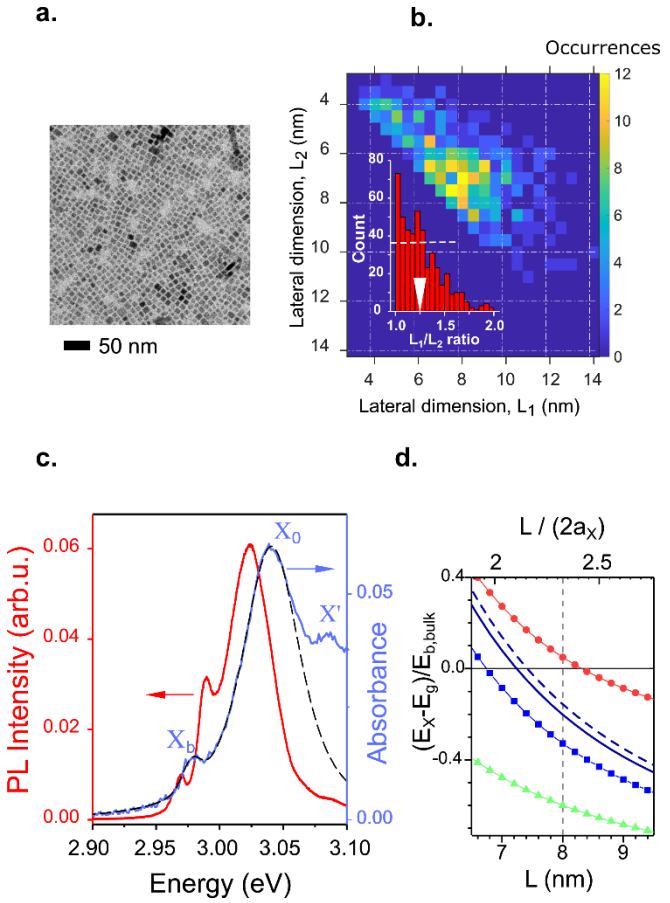

Figure 1. Optical properties and structural - size and shape - analysis of the $CsPbCl_3$ perovskite nanocrystals (NCs). **(a)** TEM image of the $CsPbCl_3$ perovskite NCs addressed in the study. **(b)** 2D, lateral sizes (L_1 and L_2, $L_1 \geq L_2$), distribution histogram (main panel) and L_1/L_2 distribution reduced histogram (lower-left corner inset). The white dash line provides the FWHM of the distribution (white tip), estimated around 1.20 ± 0.05 in the samples. **(c)** Absorption (blue) and PL (red) spectra of a moderately diluted phase of NCs dispersed on a glass coverslip (T = 7 K). The dashed line is a bimodal adjustment of the absorbance curve. **(d)** Exciton transition energy, $E_X - E_g$ (in unit of the bulk exciton binding energy, $E_{b,bulk}$) as a function of the absolute edge length, L (and $L/2a_X$ parameter), in cubic-shape $CsPbCl_3$ NCs (E_g = 3.056 eV, $E_{b,bulk}$ = 64 meV and a_X =1.72 nm): (i) variational calculation for three values of the dielectric mismatch, η = 0 (solid squares), η = 0.53 (solid line) and η = 0.74 (dashed line); (ii) estimations using the formula of the strong and weak confinement limits for η = 0 (solid circles and triangles respectively).[56]

Following the size analysis, the consistency between the average properties and ensemble optical responses (reflected by the absorption) - can be checked. The optical spectra presented in Figure 1c are typical of $CsPbCl_3$ NCs 'moderately' diluted phases, prepared on thin glass substrates (drop casting method) and measured at low temperature (T = 7 K). The band edge absorption is dominated by a strong peak, X_0, centered at 3.04 eV while a weaker intensity peak, X' is detected at higher energy (≈ 3.086 eV) and a satellite, X_b, is identified at lower energy (≈ 2.98 eV). The results of simulations are reported in Figure 1d. $\langle L \rangle$ ≈ 8.0 ± 0.5 nm provides a ratio $\langle L \rangle / 2a_X$ = 2.33, a_X being the exciton Bohr radius (see Supporting Information, Table S.1) that requires to consider excitons in the intermediate confinement regime (see Supporting Information SII.1 and SII.2 for description of the model). The transition energy is plotted as a function of the size (cubic

shape) and dielectric contrast parameter, η, defined as $\eta = (\varepsilon_1 - \varepsilon_2)/(\varepsilon_1 + \varepsilon_2)$, ε_1 (ε_2) being the dielectric constant inside (outside) the NC. When considering an edge length $L = \langle L \rangle$ = 8.0 nm, $\varepsilon_1 = 6.6$ and ε_2 = 2 (i.e. η = 0.53) that is consistent with a NC coated by organic ligands, one finds $E_X \approx 3.043$ eV, in good agreement with the value found in the experiments for the X_0 peak position. Only slight variations of the exciton transitions (few meV) are obtained as the dielectric contrast is varied; they may add to the energy fluctuations associated to the size dispersion to explain the broadening of the absorption peak. At higher energy, X' has not been clearly identified yet but is probably associated to an excited exciton transition (2s exciton or exciton built from p-states). Larger size NCs form the tail of the distribution and more likely contribute to the low energy structure, X_b, noting that free excitons transitions were clearly identified in crystalline films (2.992 eV at 2 K)[16,57] or macro-crystals (2.985 eV and 3.010 eV at 13 K)[58].

In perovskite materials and NCs the band gap energy is governed by the Pb s to the halide p covalent antibonding interaction that translates into a blue shift of the transitions with increasing temperature.[59] Here the X_0 and X_b resonances obey a usual Varshni relation with a negative expansion coefficient of a few tenths of meV/K and a low Debye temperature. These parameters are typical of perovskite materials (See Supporting Information, S.I).

The photoluminescence (PL) spectrum is significantly Stokes-shifted with regard to the absorption (red shift $\Delta E_{SS} \approx 16$ meV). The origin of the Stokes-shift in perovskite NCs is a debated topic but it is known to be intrinsic to the electronic structure and increases with the confinement. The value found here matches the one reported by Brennan and co-authors for $CsPbCl_3$ NCs with $\langle L \rangle \approx 8.0$ nm.[60] The 'central' sharper structure peaks at 2.99 eV, an energy that corresponds to a 25 meV shift from the main exciton peak X_0. The difference matches the LO_2 phonon quantum energy evidenced in several studies meaning that a phonon replica line is likely observed.[61-63]. Following the absorption analysis, the lower energy PL peak can be seen as the emission line associated to X_b. The lower Stokes-shift with respect to X_b ($\approx$ 8 meV) is the indication of the poor level of confinement that subsists in the objects responsible for this emission.[60]

Photoluminescence Micro-Spectroscopy. As a next step, we consider the influence of the coupled influence of symmetry, size, shape anisotropy and dielectric confinement strength on the EFS. To be able to address the EFS of single $CsPbCl_3$ NCs, the surface density of NCs on the substrates is drastically reduced (dilution factor of 10^3 typically, with respect to the concentration used to measure the spectrum of Figure 1c) and the NCs emission is imaged using a home-built confocal-like microscope coupled to the optical spectrometer ($\approx$ 100 µeV energy resolution, spatial resolution $\leq$ 1 µm). In micro-PL experiments, single $CsPbCl_3$ NCs responses are clearly identified under the form of sharp spectroscopic lines forming either doublets or triplets (bright states EFS) characteristic of hybrid or purely inorganic lead-based perovskite particles PL.[43,51,52,55]

Providing an explanation about the mechanisms shaping the EFS remains a challenge for it requires, in principle, that the absolute crystalline structure of the NC is known. Theoretical predictions however allow to establish correlations between the spectroscopic patterns and possible intrinsic structural and symmetry features. If the NC is of cubic shape, the EFS is basically determined by an interplay of the symmetry of the crystalline phase and electron-hole exchange interaction. Then doublets (having one degenerated component) are representative of the tetragonal (D_{4h} point group) symmetry and triplets – resulting from a complete lifting of the EFS states degeneracy - should be associated to the orthorhombic (D_{2h}) structure.[51,52,64] This schematic picture has to be revisited as the NC shape anisotropy is introduced ie as soon as the geometry departs from a pure cube with triplets that might be generated already in the tetragonal phase if NC deformations are applied along particular directions (the point is discussed in detail thereafter).

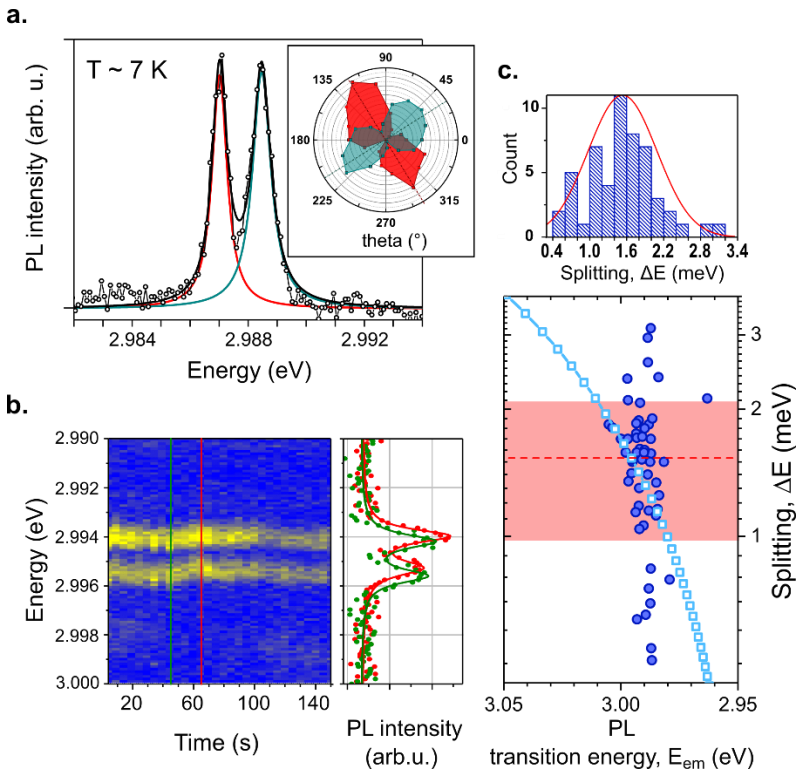

Figure 2. (a) Typical single $CsPbCl_3$ NC response as a doublet, measured at 7 K. The black solid line is a two-components (red and blue solid lines) Lorentzian fit. Inset: polar diagram of the PL intensity. **(b)** Time evolution of a single NC PL (3 s integration time per spectrum, no polarization selection) and two cross-sections (side-graph). **(c)** Upper panel: histogram of the splitting energy values, ΔE, and its adjustment to a normal distribution (solid red line). Lower panel: ΔE as a function of the PL transition energy, E_{em}: experimental points (solid circles) and theoretical predictions for cubic-shape NCs in the intermediate confinement regime (open squares); note that the theoretical $\Delta E = f(E_{em})$ curve is obtained by shifting the absorption curve (to account for the PL Stokes-shift) so that $E_X(L = \langle L \rangle = 8$ nm) matches the mean energy of the experimental distribution. The red dashed line is a marker for the average splitting value ($< \Delta E > \approx 1.53$ meV) whereas the colored band indicates the one sigma standard deviation (SD) associated to the ΔE value distribution (SD ≈ 0.56 meV).

In this study we note the strong proportion of doublets that represent more than 85 % of the detected patterns. A typical spectrum is presented in Figure 2a along with the polarization analysis of the structure (polar plot in the inset) indicating the crossed polarized nature of each component which linewidths have been measured between 0.6 and 1 meV (well above the ≈100 µeV experimental energy resolution). Under the influence of local electric fields, a concerted shift of the EFS peaks is clearly observed, demonstrating the intra-particle nature of the measured optical response. Figure 2b provides insights into the level of stability characteristic of the excitonic transitions. With an amplitude of 300 - 500 µeV in the shifts, the spectral diffusion has a broader impact than in bromide and iodide systems, also likely explaining that significantly larger EFS peaks linewidths (comparatively ≈ 2 times larger) are measured for $CsPbCl_3$ NCs at 7 K.[48,51,52]

In the literature, the case of $CsPbCl_3$ was under focus within two studies.[62,65] In Bertolotti's work NCs (~ 10 nm edge length) are modelled as the assembly of orthorhombic monodomains at low temperature (T ~ 130 K),[65] whereas a tetragonal phase was found to match the XRD patterns of larger NCs (size ~ 20 nm) at 80 K.[62] The observation of doublets (the analysis of polarization allowing to discard the presence of any additional structure in the spectrum) has however a strong and direct implication here, that is NCs in the tetragonal system should be considered as the majority population in the studied batch even if the coexistence of lower symmetry NCs cannot be

excluded (the coexistence of two phases was evidenced in the $CsPbBr_3$ compound).[51,52] So, starting from the experimental premise that doublets are observed, an interpretation that allows to clarify the occurrence of various micro-PL patterns postulating the same origin with regard to the structural properties is privileged. The analysis will thus be conducted in the hypothesis of NCs being primarily in the tetragonal phase.

Then the EFS is theoretically modelled including the short range (SR) and long range (LR) contributions of the e-h EI within an approach comparable to the one developed in bromide-based NCs.[66,67] In the model the electron-hole Coulomb interaction potential serving to express the LR term is evaluated in the image charges formalism, which allows to describe in an extensive manner the effects of dielectric confinement in the actual parallelepiped NCs geometry. Following the calculations, the EFS can be addressed through the set of equations (S23) - (S24) for any size, shape (ie anisotropy level), dielectric mismatch configurations in the cubic (O_h) and tetragonal (D_{4h}) crystal phases. In agreement with previous studies[31,56,67,68] the inspection of equations (S23) shows that, in halide perovskite NCs with tetragonal lattice structure, both SR and LR contributions participate in the singlet (dark state) – triplet (bright state) and intra-triplet (intra-bright states) splitting with comparable strength. The shape distortion and dielectric discontinuity play a role under the form of weighting coefficients that modulate the amplitude of the LR Hamiltonian unperturbed eigen energies (cubic shape, no dielectric contrast).

In Figure 2c the splitting energy, ΔE, is plotted versus the PL transition energy (collection of 53 NCs) and compared to the theoretical expectations assuming NCs of purely cubic-shape and considering an outside dielectric constant, $\varepsilon_2 = 2$. Note that in the figure, the emission energy, E_{em}, is translated from E_X by an amount of ≈ 40 meV to compensate for the PL Stokes-shift (see above); the curve was thus placed so that the transition in absorption, $E_X(L = \langle L \rangle = 8$ nm), matches the mean energy of the experimental splitting distribution associated to the doublets ($< \Delta E > \approx 1.53$ meV). Despite the arbitrary character of the energy shift, the latter allows a better insight into the comparison predictions – experiments with regard to the $\Delta E = f(E_{em})$ relation (for purely cubic NCs). The graph indeed evidences a strong dispersion of the ΔE values (0.51 meV < ΔE < 3.11 meV in the 2.98 – 3.00 eV interval) and despite a reasonable agreement regarding a sub-part of the experimental sample, the striking point is that there is a general poor correlation between the splitting amplitude and the emission energy; in particular, strong deviations from the theoretical curve are observed since the larger splittings can also be measured for NCs presenting the lower transition energies. It is thus necessary to invoke an additional parameter that might be responsible from the pronounced dispersion in ΔE while having a poor influence on the transition energy. We see below that considering a slight anisotropy in the NCs shape is a straightforward solution and that it allows to explain the diversity of the individual NC PL responses, as well as the unexpected occurrence of triplets within the hypothesis of NCs in the tetragonal phase.

In Figure 3 the EFS of a tetragonal lattice NC is mapped as two types of deformation are applied while keeping the NC volume, V, constant with $V = \langle L \rangle^3$; the shape anisotropy parameters are r and s defined according to $L_Z = sL_X$ and $L_Y = rL_X$ (the volume being kept constant, the edge lengths read $L_X = \langle L \rangle (rs)^{-1/3}$, $L_Y = \langle L \rangle r^{2/3} s^{-1/3}$ and $L_Z = \langle L \rangle r^{-1/3} s^{2/3}$). r=s = 1 thus defines a NC of perfect cubic shape. In the following two schemes are considered: (i) the NC is distorted by varying the s parameter but maintaining r = 1 which means that the crystal is elongated/contracted along the $\boldsymbol{c}$ axis of the tetragonal phase but keeps a square-like section in the (XY) plane orthogonal to $\boldsymbol{c}$ (panel a) or, (ii) r varies while s = 1, that corresponds to a distortion in the plane orthogonal to $\boldsymbol{c}$ (panel b), with a square-like section maintained in the (XZ) plane containing the $\boldsymbol{c}$ axis direction. Considering distortions along the highest symmetry axis, $\boldsymbol{c}$, already explains much of the experimental features and is described first. A crucial result is that a doublet ($|Z\rangle$ state and ($|X\rangle$, $|Y\rangle$) twofold degenerate states) is always observed (except at the curves

crossing where the three states are degenerate). A contraction along $\boldsymbol{c}$ leads to a continuous increase of the energy spacing, $\Delta E_{Z,XY}$, between the highest energy $|Z\rangle$ state and the degenerate ($|X\rangle$, $|Y\rangle$) pair. $\Delta E_{Z,XY}$ is doubled (from 1.42 meV to 2.79 meV) as L_Z experiences a ≈ 20 % decrease (s passing from 1 to 0.82 respectively). A doublet that possibly matches is displayed in Figure 3c. Conversely, a decrease in $\Delta E_{Z,XY}$ is predicted as an elongation is applied ($s > 1$) and the threshold above which a state inversion occurs is expected around $s = s_0 = 1.25$ in $CsPbCl_3$ NCs. The reported dispersion in ΔE displayed in Figure 2c is thus reproduced as s spans a wide interval (possibly with $s > s_0$) compatible with the actual 'distribution of anisotropy' (Figure 1b).

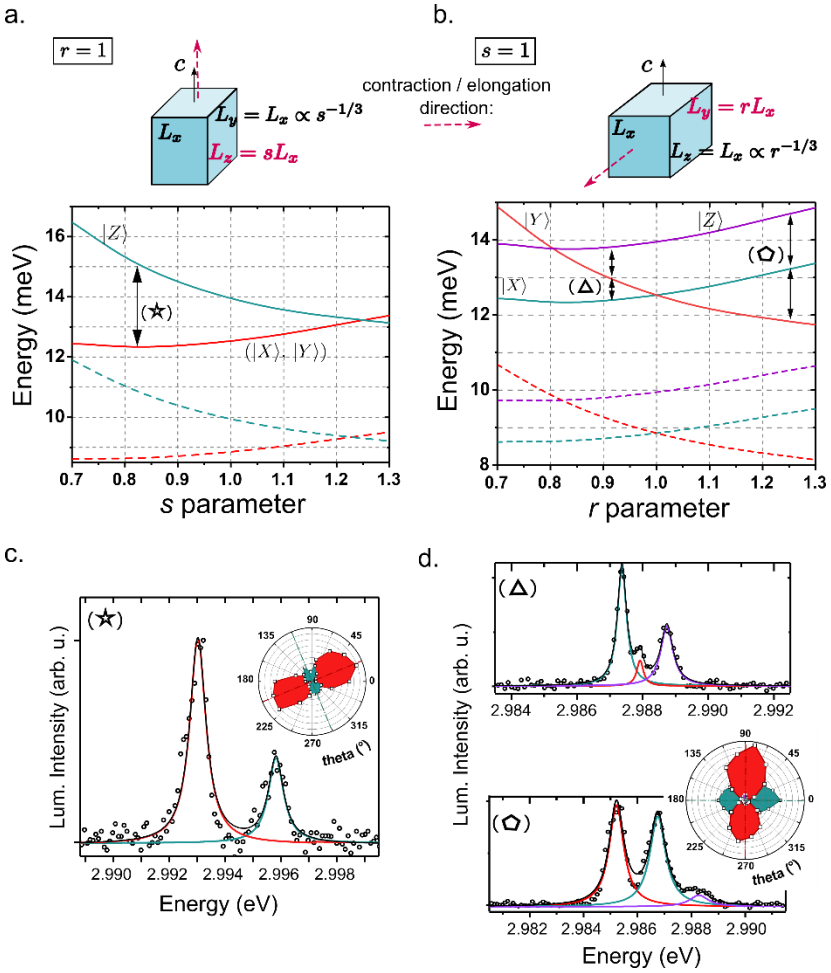

Figure 3. Exciton fine structure (triplet bright state) in parallelepiped shape NCs (tetragonal lattice) whose volume is held constant: $L_X = \langle L\rangle(rs)^{-1/3}$, $L_Y = \langle L\rangle r^{2/3}s^{-1/3}$ and $L_Z = \langle L\rangle r^{-1/3}s^{2/3}$. **(a)** Shape distortion along the tetragonal, high symmetry, $\boldsymbol{c}$ axis for two values of the dielectric mismatch η: $\eta = 0.53$ or $\varepsilon_2 = 2$ (solid lines) and $\eta = 0$ or $\varepsilon_2 = 6.56$ (dashed lines); the EFS consists of a $|Z\rangle$ state linearly polarized along $\boldsymbol{c}$ and a degenerate doublet, ($|X\rangle$, $|Y\rangle$) having their dipoles in the plane orthogonal to $\boldsymbol{c}$. **(b)** Shape distortion in the plane orthogonal to the $\boldsymbol{c}$ axis: $\eta = 0.53$ (solid lines) and $\eta = 0$ (dashed lines); the EFS consists of three orthogonal and linearly polarized states, $|X\rangle$, $|Y\rangle$, and $|Z\rangle$. In panels (a) and (b) the volume is held constant ($V = \langle L\rangle^3$, $\langle L\rangle = 8$ nm) when changing the edge lengths according to $L_Z = sL_X$, $r = 1$ (panel (a)) and $L_Y = rL_X$, $s = 1$ (panel (b)); in the upper pictograms, the arrows in magenta indicate the deformation direction. Note also that the zero-energy reference corresponds to the singlet dark state position. **(c)** Doublet emission with a relatively large splitting, $\Delta E = \Delta E_{Z,XY} = 2.79$ meV, that is possibly associated to $s = 0.82 - \eta = 0.53$ most appropriate value – in the graph of panel (a) (see star symbol). Inset: polarization diagram of the emission. **(d)** Two triplet structures corresponding to geometries obtained via the deformation operation described in panel (b): $r = 0.91$ (up triangle) leading to the splittings $\Delta E_{Z,Y} = 0.62$ meV, $\Delta E_{Y,X} = 0.58$ meV and $r = 1.25$ (pentagon) leading to equidistant peaks with $\Delta E_{Z,X} = \Delta E_{X,Y} = 1.52$ meV. The polarization diagram was measured for one of the two triplets only.

The observation of small splittings (ΔE of the order of 0.5 meV) additionally raises the question of a finer characterization of the doublet structures in the region around $s = s_0$ (in particular to identify the position of the non-degenerated $|Z\rangle$ state in the doublet). Such investigations, that require magneto-optical techniques[51] in order to lift the ($|X\rangle$, $|Y\rangle$) degeneracy, were not practicable in the course of the study.

The energetic landscape becomes more complex as the deformation is envisaged in one of the directions orthogonal to the $\boldsymbol{c}$ axis (see Figure 3b); the inclusion of the shape asymmetry when evaluating the LR part of the e-h EI manifests itself in the complete lifting of the EFS triplet in the same way the lowering of symmetry operates in a cube shape crystal when moving from the tetragonal to the orthorhombic phase.[51,68] The main effect is thus the emergence of the triplet pattern ($|X\rangle$, $|Y\rangle$, and $|Z\rangle$ states) with orthogonally polarized lines as soon as r differs from 1 (with exceptions of crossing points for which a doublet remains). In Figure 3d, we provide two illustrations possibly associated to $r = 0.91$ (peak separation of the order of the natural linewidth) and $r = 1.25$ (larger peak separation). It should be pointed out that triplets might also be associated to NCs in the orthorhombic phase with an 'EFS configurations space' that is large (the study of Han et al. for $CsPbI_3$ provides a complete picture, incorporating the effect of anisotropy)[69] but only single object correlative spectroscopy (high resolution electron microscopy vs optical micro-PL) could allow to distinguish the different origins for the characteristic triplet-like response.

Before investigating PL in time resolved experiments, let us focus on a couple of points: (i) Even for a perfectly cubic-shape NC, the fluctuations in the dielectric environment may already lead to appreciable variations in the doublet splitting energies, ΔE, thus contributing to their dispersion. We estimate that a reasonable variation in ε_2 (outside dielectric constant) from $\varepsilon_2 = 3.0$ ($\eta = 0.37$) to $\varepsilon_2 = 1.0$ ($\eta = 0.74$) leads to ΔE values ranging between 1.33 and 1.52 meV (average volume, $V = \langle L \rangle^3$, $\langle L \rangle = 8$ nm). Those are too small values to explain the experimental dispersion. Moreover, within the frame of a tetragonal lattice, the observation of triplets cannot be explained otherwise than by introducing a specific asymmetry in the NC shape. Both arguments comfort the idea that the anisotropy is a crucial parameter and plays an effective role in shaping the EFS. (ii) Despite the limited statistics it also seems that the occurrence ratio is strongly in favor of doublets that might indicate the preferential character of the anisotropy manifestation with respect to the space directions in $CsPbCl_3$ NCs. (iii) More triplet configurations (also compatible with our experimental results) can be revealed if a concerted deformation is operated i.e. if the constraint $rs = 1$ is added in the calculations (see Figure S5). (iv) Splittings below 0.5 meV (typically, $1.2 < s < 1.3$) were not observed in our scans whereas, at first sight, they are expected. There are plausible reasons for that. Han and co-authors show that a model of NCs with pseudocubic bounding facets changes the LR exchange interaction so that the $|X\rangle$ and $|Y\rangle$ EFS states get coupled and acquire an avoided crossing in their energy spectrum.[69] Though noteworthy, the model requires that the crystalline phase is orthorhombic, which cannot be an initial postulate here. A possible explanation is that the actual edge lengths distribution (on its sides) might not be strictly the same as the one characterized through the TEM image analysis, as a consequence of the dilution process required to reach the spatial dispersion compatible with single object experiments. Finally, the connection between the s parameter (as defined in the theory – $L_z = sL_x$- and used in figure 3a) and the information provided in the histogram (Figure 1b) is not straightforward. The L_1 and L_2 edge lengths of the histogram cannot be absolutely identified ie associated to any of the x, y or z directions. So, the histogram only provides a global view of the anisotropy level that might be encountered in the sample without discriminating between the s and r parameters. It is not impossible that the tails in the histogram are not representative of the s parameter, which value would actually cover a narrower interval. For the same reason it is not possible to know whether a

point in the histogram addresses s or $1/s$ and it is possible that NCs with $s \leq 1$ are over-represented in the actual sample.

Time-Resolved Photoluminescence (TRPL). To gain further insights into the emission properties, the energy position of the optically inactive (ie dark) state within the EFS should be clarified. Although the most straightforward and unequivocal strategy relies on evidencing the dark state spectroscopic signature in magneto-optical experiments performed at the single NC scale,[45,49] for $CsPbCl_3$ NCs, a bright-dark splitting (Δ_{BD}) is expected in the ≈ 10 meV range (see Figure 3a,b) meaning that B fields of high amplitudes would be necessary to achieve a significant transfer of oscillator strength towards the dark state and allow its detection. The ratio between the emission intensity of the dark and bright excitons follows a quadratic law in $(\delta g \mu_B B)/\Delta_{BD}$, with μ_B the Bohr magneton, $\delta g = g_e - g_h$ with $g_{e(h)}$ the electron (hole) Landé factor and B the amplitude of the applied field (Supporting Information, S.III.1, eq. (S30)). According to the recent study of the Landé factors dependence on the gap energy,[70] one expects, for $CsPbCl_3$, $|\delta g| \leq 0.4$ An intensity ratio of 1 % leads, for Δ_{BD} = 10 meV, to a magnetic field B > 86 T. A very large magnetic field is thus required to evidence any emission from the dark state, making the TRPL experiments the most accessible and immediate strategy to reach a reliable Δ_{BD} estimation. For comparison, Tamarat *et al.* have evidenced the dark exciton emission in $FAPbBr_3$. With $\delta g \approx 2$ and Δ_{BD} = 2.6 meV, the criteria $\frac{I_D}{I_B}$ = 1 % leads to B = 3.5 T. At the maximum field used in their study (B = 7 T), the ratio is equal to 7 %, in good agreement with the spectra.[45]

The less direct approach based on the analysis of the emission dynamics and its evolution with temperature (thermal mixing model) is therefore considered instead. In this work, the model using two phonons to connect the bright and dark sub levels (and transfer populations between them) is considered (see Supporting Information, S.III.2) for it leads to a reasonably correct adjustment of the data (see below).[43,71] As the PL yield for $CsPbCl_3$ is too low to have an access to single NC dynamics a compromise is also found by investigating highly diluted films and addressing the dynamics of lines with reduced inhomogeneous broadening; this way, experiments are made combining a satisfactory signal to noise ratio and an acceptable level of averaging (over the NCs sizes) across the considered PL linewidth. Typically, lines centered around 3.025 eV (maximum of the macro-PL) were selected such that their FWHM remains below 40 meV, thus ensuring that only NCs with a $\Delta L \approx 2$ nm around the mean edge length $< L >$ = 8 nm in the cubic shape approximation (Figure 1d) contribute to the emission response. First, we notice the biexponential character of the PL decays, that is observed distinctly in the 40 K – 150 K interval typically (Figure 4a), as the central feature. In the following Γ_f and Γ_s will denote the rates associated to the fast and slow components of such decays. As shown in Figure 4b, both Γ_f and Γ_s exhibit pronounced and characteristic variations as the temperature is raised. Despite Γ_s suffers from a certain amount of dispersion, we see below that a reliable estimation of Δ_{BD} is obtained as the adjustment of Γ_f and Γ_s as a function of temperature is carried out.

To adjust the $\Gamma_{f,s}$ curves, five parameters have to be optimized: they are the intrinsic lifetime of the bright and dark states (Γ_B and Γ_D, respectively), the longitudinal optical phonon energies which difference defines Δ_{BD} and the two-phonon mixing rate, γ_0, that appears in the direct and back transfer rates expressions ($\gamma_\downarrow$ and $\gamma_\uparrow$ respectively) that are themselves determined under the hypothesis that the phonon bath is at thermal equilibrium.[43] At low temperature Γ_B identifies with Γ_f so that it is unambiguously extracted from the data. In the following we take $\Gamma_B \approx 0.028$ ps^{-1} as the average of the Γ_f values measured at 7 K, in good agreement with results from other studies in NCs ensembles.[72] In the model, $\Gamma_f \rightarrow \Gamma_D$ in the low temperature limit ($k_B T \ll \Delta_{BD}$). Throughout

this work Γ_s could not be measured below 35 K consequently an absolute determination of Γ_D cannot be done exploiting the asymptotic behavior of Γ_s. Fortunately, the values extracted from the adjustment procedure presented thereafter are found quasi-unsensitive to Γ_D variations provided it is lower than $\approx 10^{-4}$ ps^{-1}. As a consequence, an upper value $\Gamma_D \approx 2.0\ 10^{-5}$ ps^{-1} will be used as it is the highest value that allows to incorporate the extremum Γ_s point in the fitting curve.

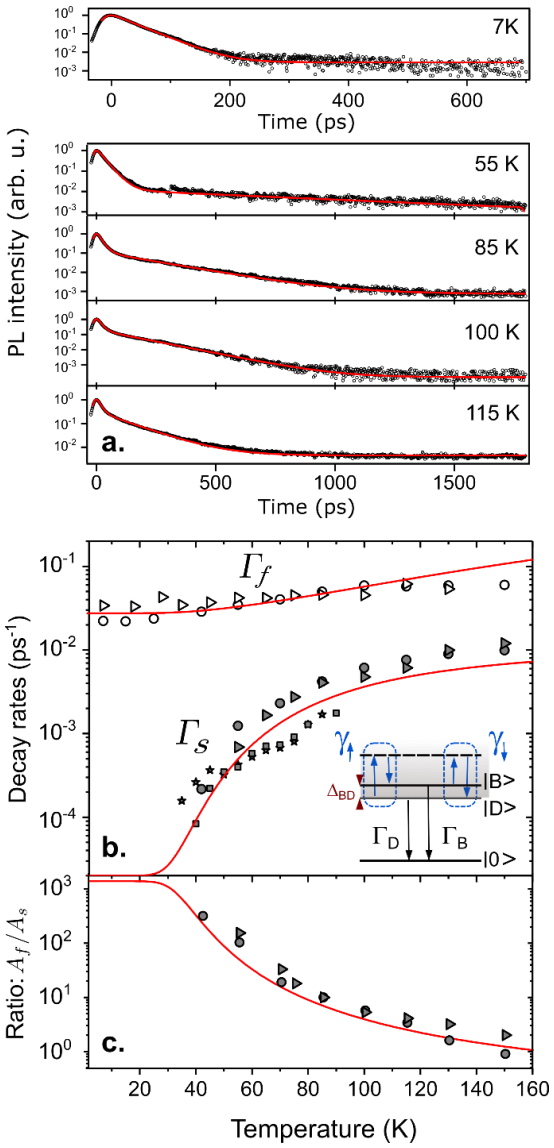

Figure 4. (a) Evolution, as a function of the temperature, of $CsPbCl_3$ NCs PL dynamics measured around the maximum of the macro PL and associated biexponential adjustments (red solid lines) according to $I_{PL}(t) = A_F e^{-\Gamma_f t} + A_s e^{-\Gamma_s t}$. **(b)** Variation of the Γ_f and Γ_s rates as a function of temperature. Each symbol refers to a set of measurements covering the 7 K - 155 K range. Open and filled symbols are respectively for the fast and slow components of the same decay. All PL decays were recorded using a streak camera except two series in which it was resorted to TCSPC to characterize Γ_s (filled grey-shaded squares and stars). The red solid lines are the best simultaneous adjustments of the Γ_f and Γ_s rates (7 K – 115 K interval) including all the available data in the fitting procedure. Inset: Scheme of intra-EFS couplings in the two-phonon kinetic model. **(c)** Ratio of the fast and slow component amplitude factors, A_f/A_s, as a function of temperature: comparison between the experimental data (symbols) and the evolution simulated using the parameters extracted from the adjustment procedure of Γ_f and Γ_s rates (red solid line).

The LO-phonon of lower energy was chosen in agreement with the results of Raman measurements performed on the chloride material ie $E_{ph\ low}$ is set to 14.3 meV.[61] From that point the concerted adjustment of Γ_f and Γ_s leads to $\Delta_{BD} \approx 10.7 \pm 3.0$ meV (ie $E_{ph\ up} \approx 25.0 \pm 3.0$ meV) and $\gamma_0 \approx 0.10 \pm 0.01$ ps^{-1} when including all the (Γ_f, Γ_s) pairs within the [7-115 K] range so as to avoid the drop in Γ_f above 120 K that is not consistent with the model predictions (see fit in Figure 4b). The Δ_{BD} estimation is thus in good agreement with the theoretical results that predict an energy distance of 13.2 meV between the dark state and the center of the bright doublet in a cubic shape NC with an edge length, L, of 8 nm (Figure 2a). The global consistency of the approach is also supported (i) first, by the proximity of $E_{ph\ up}$ and the energy of the LO phonon identified by Calistru and co-authors, in the bulk, at 27.8 meV,[61] and more recently around 25 meV, in NCs,[62,63] so that the 'bright – dark coupling' is mediated by a two phonons process operating close to resonance, explaining the relatively large value obtained for γ_0;[71] (ii) second, and in a complementary manner, by the experimental variation, of the ratio A_f/A_s (fast *vs* slow component weight in the PL decay). With a good approximation, the ratio indeed also matches the evolution predicted by the dark to bright states back transfer thermally activated model (Figure 4c) ; (iii) finally, it was checked that the whole PL intensity is maintained nearly constant in the studied interval (see Supporting Information, S.III.3), allowing to perform the analysis by keeping the Γ_B and Γ_D rates independent on temperature, Γ_B and Γ_D incorporating both the radiative and non-radiative components of the relaxation.

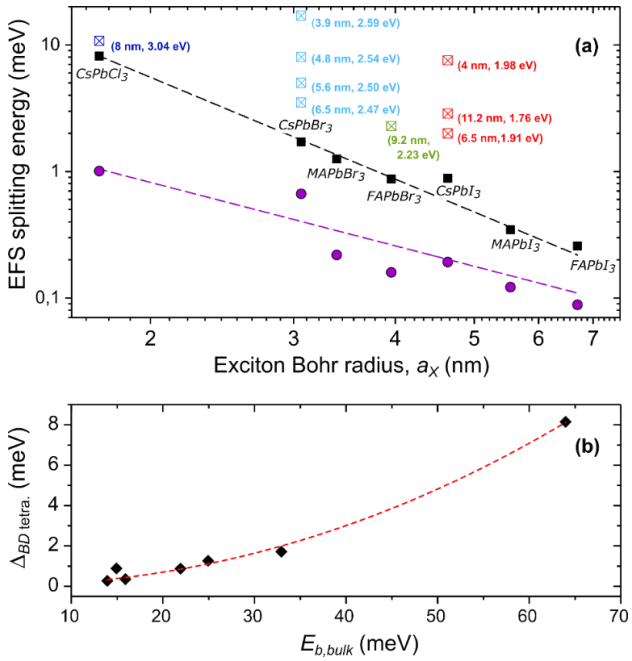

Figure 5. (a) Calculated bright-bright, Δ_{BB}, (filled circles) and bright-dark, Δ_{BD}, (filled squares) energy splittings as a function of the exciton Bohr radius, a_X, in hybrid and fully inorganic lead-halide perovskite materials. All materials are treated in the same limit used as a reference: weak confinement limit of NCs (edge length, $L \gg a_X$), $\eta = 0$ and isotropic shape. Adjustments using power laws (dashed lines) are also shown: $\Delta_{BB} = c_{BB}(a_X/a_0)^{\kappa_{BB}}$ and $\Delta_{BD} = c_{BD}(a_X/a_0)^{\kappa_{BD}}$ (c_{BB} = 2.56 ± 0.70 meV, κ_{BB} = -1.66 ± 0.33, c_{BD} = 35.0 ± 1.9 meV, κ_{BD} = -2.67 ± 0.09 and a_0 = 1 nm). The values are summarized in Table I as well as the physical parameters used for the calculations. For comparison, experimental Δ_{BD} values for NCs are also reported (cross tagged squares) as well as the associated NC size (edge length) and exciton transition energy (text labels), for $CsPbI_3$,[49,73] $FAPbBr_3$,[45] $CsPbBr_3$[73] and $CsPbCl_3$ (this work). **(b)** Plot of the dark state - bright state splitting, Δ_{BD}, as a function of the exciton binding energy (weak confinement limit, η = 0, isotropic shape): the dashed

line is an adjustment proposal using a power law according to $\Delta_{BD} = c_1 \left(E_{b,bulk}/E_b^0\right)^{c_2}$ with c_1 = 1.2 ± 0.6 10^{-3} meV, c_2 = 2.1 ± 0.1 and E_b^0 = 1 meV.

Due to the influence of several parameters on the NC EFS (absolute size, anisotropy level, nature of the dielectric environment) drawing a comparison between the existing compounds should be made with great caution. As stressed in a recent theoretical work, Δ_{BD} is especially sensitive to the dielectric mismatch and almost insensitive to the shape anisotropy whereas Δ_{BB} has schematically the opposite behavior.[67] In that respect a good starting point for discussion consists in investigating a reference situation allowing comparison. The latter is defined as the weak confinement limit of excitons (ie large NCs with edge lengths, L, such that $L \gg a_X$) in NCs of isotropic shape and in absence of dielectric mismatch. In this limit and in a model describing the EFS through the e-h EI and crystal field combined effects (see Supporting Information, S.II), both Δ_{BD} and Δ_{BB} (splitting between the exciton bright states under the effect of a tetragonal field) increase as the exciton Bohr radius (binding energy) decreases (increases). Figure 5a-b shows the trends for different halide perovskites, with energy splittings calculated using the equations set (S24) and data of Table I. It is important to precise that the considered limit cannot be representative of the bulk situation that requires the theory of the EI to be formulated by incorporating k-dispersion.[27,29,56]

Table I. Physical parameters used in calculating the EFS splittings in the weak confinement limit in absence of dielectric mismatch (η = 0) and for NCs of isotropic shape.

D_{4h}	E_g (eV)	ε_1	ε_X	a_X (nm)	$E_{b,bulk}$ (meV)	μ	θ (°)	Δ_{SR} (meV)	$E_{P_{S,z}}$ (eV)	$E_{P_{S,\rho}}$ (eV)	Δ_{BD} (meV)	Δ_{BB} (meV)	$\Delta_{BD,SR}$ %	$\Delta_{BB,SR}$ %
$FAPbI_3$	1.501	11.4	6.4	6.7	14	0.090	39.76	0.076	18.25	19.04	0.26	0.09	26	29
$MAPbI_3$	1.653	10.9	6.6	5.5	16	0.104	40.06	0.134	15.36	16.45	0.35	0.12	34	40
$CsPbI_3$	1.738	10	4.3	4.6	15	0.114	39.56	0.229	17.03	19.81	0.88	0.19	23	39
$FAPbBr_3$	2.233	8.6	5.7	4.0	22	0.115	37.67	0.369	19.75	20.01	0.87	0.16	40	42
$MAPbBr_3$	2.292	7.5	5.6	3.4	25	0.117	38.14	0.586	16.45	17.97	1.25	0.22	43	58
$CsPbBr_3$	2.342	7.3	4.5	3.1	33	0.126	40.4	0.793	15.65	16.8	1.71	0.66	40	47
$CsPbCl_3$	3.056	6.6	4.1	1.7	64	0.202	37.65	4.422	15.24	17.21	8.15	1.01	51	79

E_g: energy gap;[16] ε_1: bulk dielectric constant; ε_X: dielectric constant at the exciton resonance; a_X: exciton Bohr radius; $E_{b,bulk}$: exciton binding energy;[16] μ: exciton reduced mass;[16] θ: Bloch function parameter (see section S II.3);[31,42] Δ_{SR}: bulk short range (SR) splitting parameter (calculated using $\Delta_{SR} = \frac{2}{3}\frac{C}{\pi a_X^3}$, C = 107.6 meV.nm^3 [31]); $E_{P_{S,\rho}}$ and $E_{P_{S,z}}$: Kane energies; [31,42] Δ_{BD} and Δ_{BB}: bright-dark and bright-bright EFS splittings respectively of excitons in the weak confinement limit in absence of dielectric mismatch and for an isotropic shape (ie edge lengths, $L \gg a_X$), calculated with eq. (S24). Note that ε_1, ε_X, $a_X = \frac{\epsilon_1 a_0}{\mu}$ (a_0 = 0.529 Å), $E_{P_{S,\rho}}$, $E_{P_{S,z}}$ and θ values are specific of the material tetragonal phase. $\Delta_{BD,SR}$ ($\Delta_{BD,LR}$): contribution of the short range (long range) term to the Δ_{BD} (Δ_{BB} respectively) EFS splitting.

Adjustments of the EFS splittings as a function of a_X assuming power laws, provide an exponent κ_{BD} = -2.67 ± 0.09 for Δ_{BD} while a lower value is found for κ_{BB} with κ_{BB} = -1.66 ± 0.33 (and with a larger dispersion in the experimental set). Both splittings are made of two contributions associated to the long range (LR) and short range (SR) parts of the e-h EI. In the expression of Δ_{BD} (eq. (S24)), the SR contribution is proportional to the short range parameter, Δ_{SR}, shown to scale with a quasi-universal a_X^{-3} dependence regardless of the considered semiconducting

material.[31] By contrast the LR component of Δ_{BD} does not show the a_X^{-3} law. Moreover, the ratio of the SR term in the whole Δ_{BD} splitting varies from 23 % to 51 % when the halogen is changed from iodide to chloride in inorganic compounds (a similar evolution is observed for compounds containing organic cations). These two facts are responsible for the deviation of Δ_{BD} from the characteristic Δ_{SR} behavior ($\kappa_{BD} \neq$ -3). In Table 1 we notice the same trend for the ratio of the SR contribution to the whole Δ_{BB}.

The studied $CsPbCl_3$ NCs excitonic properties are characteristic of the intermediate confinement regime (Figure 1d and Figure S2). The experimental value for Δ_{BD} deduced from the PL dynamic study is coherently found higher in these NCs with respect to the bulk (≈ 30 % increase). As a comparison, enhancements of one order of magnitude have been observed in the iodide and chloride compounds in which a larger confinement range could be explored (Figure 5a). Finally, for a given level of confinement (ratio $< L > / 2a_X$) there is also a clear trend associated to the increase of Δ_{BD} in more tightly bound excitons. This is clearly seen when inspecting the caesium-lead serie (Figure 5) with Δ_{BD} passing from 2 meV in the iodide compound ($< L > / 2a_X \sim 0.7$) to 3.5 meV in the bromide compound ($< L > / 2a_X \sim 0.9$) to reach 10.7 meV in the chloride system (though $< L > / 2a_X \sim 2.3$ is comparatively - and adversely - much higher). The same trend is observed with regard to the evolution of Δ_{BB} even if its dependence on the shape anisotropy parameter is more pronounced and makes comparisons less straightforward. As seen in Table S.2, where results obtained for emission energies close to the bulk energy (to avoid erratic variations due to confinement and shape anisotropy effects) have been gathered, Δ_{BB} keeps increasing as the binding increases. Typically, a Δ_{BB} enhancement of nearly one order of magnitude can be evidenced – from a few hundreds of μeV in the caesium-iodide compound to 1.8 eV in the chloride system – further confirming that the band edge exciton physics in mostly determined by the exchange interaction model in those emergent classes of semiconducting materials.

CONCLUSION

In this paper the EFS properties of caesium-lead-chloride perovskite materials have been addressed in detail on the basis of highly resolved micro-spectroscopy experiments. Throughout the study the emission patterns of individual NCs could be unveiled (mostly doublets were revealed) and the quantification and analysis of the characteristic splittings associated to the EFS states, Δ_{BB} and Δ_{BD}, were conducted. The results could be interpreted in a unified and comprehensive way considering a crystal lattice of tetragonal symmetry: in particular the relatively high dispersion of the bright-bright splitting values, Δ_{BB} - that could not be assigned to size ie confinement effects exclusively - was successfully explained taking into account shape deviations from a perfect cubic nanocrystal geometry, in agreement with the shape-anisotropy level that was estimated from the structural characterization (TEM). It was demonstrated that, even a moderate deformation rate of the NC edge length, considered along or perpendicular to the crystal highest symmetry axis, is at the origin of a large distribution in Δ_{BB} values, potentially associated to a decisive re-organization of the EFS in terms of states ordering; depending on the nature of the deformation the generation of EFS triplet-like emission patterns are also predicted by the theory, the latter being also clearly evidenced in the experiments. The general agreement between the developed theoretical model and experimental output is furthermore attested thanks to the determination of Δ_{BD} through complementary time-resolved experiments performed on NCs ensembles with low size dispersion.

On the one hand, the theoretical description that gives the major role to the dielectric confinement-enhanced e-h EI (incorporating both the short and long-range terms) allows advanced predictions with regard to the EFS states organization and polarization for the chloride compound.

On the other hand, our developments also consist in a general approach suitable to the refined description of any of its lead-chloride counterparts incorporating all of the physical relevant ingredients. We note that the chloride compound is emblematic of a system supporting among the most tightly bound exciton in the lead-based perovskite family. The results obtained here (largest amplitude of Δ_{BB} and Δ_{BD}) thus improve the general understanding of the relation exciton-binding vs EFS structure in this new class of semiconductors, that is found perfectly conform to the one predicted by the e-h EI model when examining the large panel of available results in the field.

In addition to their fundamental nature, the present results might also present a general interest practically speaking. The enhanced control of the NC growing process (and resulting shape anisotropy) might indeed consists in a direct pathway towards a fine tuning of the EFS in nanophotonic applications in which a specific radiative coupling between a NC quantum source and a guide or a resonator might be desired and achieved (polarization and energy).

EXPERIMENTAL METHODS

$CsPbCl_3$ NCs synthesis.
Chemical: Lead (II) chloride ($PbCl_2 \geq 99$ %, Alfa-Aesar), caesium carbonate (Cs_2CO_3, 99 %, Alfa-Aesar), oleic acid (OA, 90 %, Alfa-Aesar), 1-octadecene (ODE, 90 %, Alfa-Aesar), oleylamine (OLA, 80-90 %, Thermo scientific).

Caesium oleate: In a 100 mL three-neck flask, 0.8 g of Cs_2CO_3 are mixed with 2.5 mL of OA and 30 mL of ODE. The flask is degassed under vacuum for the next 30 minutes at 110°C. The atmosphere is then switched to Ar and the temperature is raised to 200°C for 10 min. At this point the caesium salt is fully dissolved. The temperature is cooled down below 110°C and the flask is further degassed for 10 minutes. The obtained gel is used as stock solution.

$CsPbCl_3$ nanocrystals: In a 25 mL three-neck flask, we introduced 157 mg of $PbCl_2$ in 10 mL of ODE. The flask is degassed first at room temperature until the bubbling of the solution slowed down and then at 110°C for the next 30 minutes. We then inject 0.5 mL of OA and wait for vacuum to recover. Then 0.5 mL of OLA are also added to this reaction mixture. The degassing is further continued at 10°C for 30 min. The atmosphere is switched to N_2 and the temperature is set at 180°C. We then quickly inject 0.8 mL of caesium oleate stock solution. The reaction is conducted for 30 seconds, and appears whitish. The heating mantle is removed and the flask is cooled down using fresh air. The obtained solution is centrifuged at 6000 rpm for 5 minutes. The supernatant is discarded and the obtained pellet is redispersed in fresh hexane.

TEM characterization. A dilute NC solution was drop-casted onto a copper grid covered with an amorphous carbon film. The grid was degassed overnight under secondary vacuum. Imaging was conducted using a JEOL 2010 transmission electron microscope operated at 200 kV.

Steady-state visible absorption. Spectra have been acquired with a Cary 5000 spectrometer. Low temperature (down to ≈ 10 K) measurements were done resorting to an exchange gas cryostat inserted in the spectrometer main chamber.

Micro-photoluminescence spectroscopy. High-resolution (spatial and spectral domains) experiments are performed thanks to a home-made confocal-like setup using a large working-distance microscope objective (N.A. ≈ 0.6) to focus light on the nano-object and collect the emission in a reflection configuration. In the studies NCs are dispersed (dropcasting method) on

glass slides (thickness ≈ 100 μm) glued on the cold finger of a cryostat designed for thermal expansion compensation (from Oxford Instrument company). The PL signal is analyzed thanks to a 75 cm focal length spectrometer (Acton sp2750i, Princeton Instruments) itself coupled to a nitrogen cooled CCD (Spec10, Princeton Instruments), a combination that leads to the ≈ 100 μeV energy resolution required to identify the exciton fine structure components. To suppress scattered light and reach a satisfying signal to noise ratio, the excitation is pushed to 386 nm (SHG of a Ti:Sapphire laser, pulse width of ≈ 2 ps, 80 MHz repetition rate) and a dichroic filter (Thorlabs FELH0400) is placed in the detection path. The PL polarization is analyzed using a classical scheme: a motorized half-wave plate, positioned upstream along the detection beam path, allows to rotate the polarization of the NC emission that is analyzed using a fixed polarizer placed in front of the spectrometer slit (and the direction of which is parallel to the grating grooves in order to enhance the global response). It was carefully checked that no light was collected that would result from the excitation of the different optics (glass, coatings etc) by the relatively high energy optical beam.

Time resolved photoluminescence. The spectro-temporal PL maps are mainly measured using a streak-camera synchronized with the high repetition rate Ti:Sapphire laser (15 ps resolution, C5680 model from Hamamatsu incorporating a M5675 synchroscan unit) and coupled to the Acton spectrometer. To improve the signal dynamic that spans over more than three decades, complementary experiments are also performed resorting to the TCSPC technique (avalanche photodiode from Micro Photon Devices associated to a Picoquant TimeHarp 260 correlator board). The measurements mainly provide an access to the longer decay times of the characteristic biexponential PL decays in the low temperature emission regime ($T \leq 100$ K typically) with a lower temporal resolution (≈ 230 ps in the course of the experiments). All measurements were carried out in a confocal geometry (using the previously described setup) at low excitation power to avoid non-linear effects or NCs degradation.

ASSOCIATED CONTENT

The Supporting Information is available free of charge at xxx.

Temperature dependence of the band gap, calculation of the exciton wavefunction and exciton energy in the intermediate confinement regime, theory of the exciton fine structure in cuboid nanocrystals (and additional related data), magneto-optical coupling properties of the bright state – dark state system, review of the bright-bright exciton fine structure splittings (PDF)

AUTHOR INFORMATION

Corresponding Author

* **Thierry Barisien** – Institut des NanoSciences de Paris, CNRS - Sorbonne Université, BC 840, 4 place Jussieu, F-75005 Paris, France; Email: thierry.barisien@insp.jussieu.fr

Author Contributions

Ł V.G. and A.G. contributed equally to this work.

Notes

The authors declare no competing financial interest.

ACKNOWLEDGMENT

Authors thank Xiang Zhen Xu for performing the TEM imaging. This work was supported by the French National Research Agency (ANR IPER-Nano2, ANR-18-CE30-0023). A.G. and K.B. acknowledge the Tunisian Ministry of Higher Education and Scientific Research as well as the French Ministry of Foreign Affairs for funding through the project PHC-Utique (CMCU 22G1305). E.L. thanks the support ERC starting grant blackQD (N°756225).

REFERENCES

(1) Kojima, A.; Teshima, K.; Shirai, Y.; Miyasaka, T. Organometal Halide Perovskites as Visible-Light Sentitizers for Photovoltaic Cells. J. Am. Chem. Soc. 2009, 131, 6050-6051.

(2) Kim, H. S.; Lee, C.-R.; Im, J.-H.; Lee, K.-B.; Moehl, T.; Marchioro, A.; Moon, S.-J.; Humphry-Baker, R.; Yum, J.-H.; Moser, J. E.; Gratzel, M.; Park, N.-G. Lead Iode Perovskite Sensitized All Solid-State Submicron Thin Film Mesoscopic Solar Cell with Efficiency Exceeding 9%. *Sci. Rep.* **2012**, *2*, 591.

(3) Lee, M. M.; Teuscher, J.; Miyasaka, T.; Murakami, T. N.; Snaith, H. J. Efficient Hybrid Solar Cells Based on Meso-Superstructured Organometal Halide Perovskites. *Science* **2012**, *338*, 643-647.

(4) Tan, Z.-K.; Moghaddam, R.S.; Lai, M.L.; Docampo, P.; Higler, R.; Descher, F.; Price, M.; Sadhanala, A.; Pazos, L.M.; Credgington, D.; Hanusch, F.; Bein, T.; Saith, H.J.; Friend, R. H. Bright Light-Emitting Diodes Based on Organometal Halide Perovskite. *Nat. Nanotech.* **2014**, *9*, 687-692.

(5) Stranks, S. D.; Sbautg, H. J. Metal-Halide Perovskites for Photovoltaic and Light-Emitting Devices. *Nature Nanotech.* **2015**, *10*, 391-402.

(6) Lin, K.; Xing, J.; Quan, L. N.; de Arquer, F.P.G.; Gong, X.; Lu, J.; Xie, L.; Zhao, W.; Zhang, D.; Yan, C.; Li, W.; Liu, X.; Lu, Y.; Kirman, J.; Sargent, E.H.; Xiong, Q.; Wei, Z. Perovskite Light-Emitting Diodes with External Quantum Efficiency Exceeding 20 per Cent. *Nature* **2018**, *562*, 245-248.

(7) Zhu, H. M.; Fu, Y.P.; Meng, F.; Wu, X. X.; Gong, Z. Z.; Ding, Q.; Gustafsson, M. V.; Trinh, M. T.; Jin, S.; Zhu, X. Y. Lead Halide Perovskite Nanowire Lasers with Low Lasing Thresholds and High Quality Factors. *Nat. Mater.* **2015**, *14*, 636-642.

(8) Xing, G.; Mathews, N.; Lim, S. S.; Yantara, N.; Liu, X.; Sabba, D.; Grätzel, M.; Mhaisalkar, S.; Sum, T. C. Low Temperature Solution-Processed Wavelength-Tunable Perovskites for Lasing. *Nat. Mater.* **2014**, *13*, 476-480.

(9) Dou, L. T.; Yang, Y.; You, J. B.; Jong, Z. R.; Chang, W. H.; Li, G.; Yang, Y. Solution-Processed Hybrid Perovskite Photodetectors with High Detectivity. *Nat. Commun.* **2014**, *5*, 5404.

(10) Fang, Y.; Dong, Q. F.; Shao, Y. C.; Yuan, Y. B.; Huang, J. S. Highly Narrowband Perovskite Single-Crystal Photodetectors Enabled by Surface-Charge Recombination. *Nat. Photonics* **2015**, *9*, 679-686.

(11) Mir, W. J.; Livache C.; Goubet N.; Martinez, B.; Jagtap, A.; Chu, A.; Coutard, N.; Cruguel, H.; Barisien, T.; Ithurria, S.; Nag, A.; Dubertret, B.; Ouerghi, A.; Silly, M. G.; Lhuillier, E. Strategy to Overcome Recombination Limited Photocurrent Generation in $CsPbX_3$ Nanocrystal Arrays. *Appl. Phys. Lett.* **2018**, *112*, 113503.

(12) Kepenekian, M.; Robles, R.; Katan, C.; Sapori, D.; Pedesseau, L.; Even, J. Rashba and Dresselhaus Effects in Hybrid Organic - Inorganic Perovskites: from Basics to Devices. *ACS Nano*

2015, *9*, 11557-11567.

(13) Kepenekian, M.; Even, J. Rashba and Dresselhaus couplings in Halide Perovskites: Accomplishments and Opportunities for Spintronics and Spin-Orbitronics. *J. Phys. Chem. Lett.* **2017**, *8*, 3362-3370.

(14) Garcia-Arellano, G.; Trippé-Allard, G.; Legrand, L.; Barisien, T.; Garrot, D.; Deleporte, E.; Bernardot, F.; Testelin, C.; Chamarro, M. Energy Tuning of Electronic Spin Coherent Evolution in Methylammonium Lead Iodide Perovskites. *J. Phys. Chem. Lett.* **2021**, *12*, 8272-8279.

(15) Garcia-Arellano, G.; Trippé-Allard, G.; Campos, T.; Bernardot, F.; Legrand, L.; Garrot, D.; Deleporte, E.; Testelin, C.; Chamarro, M. Unexpected Anisotropy of the Electron and Hole Landé g-Factors in Perovskite $CH_3NH_3PbI_3$ Polycrystalline Films. *Nanomaterials* **2022**, *12*, 1399.

(16) Baranowski, M.; Plochocka, P.; Su, R.; Legrand, L.; Barisien, T.; Bernardot, F.; Xiong, Q.; Testelin, C.; Chamarro, M. Exciton Binding Energy and Effective Mass of $CsPbCl_3$: a Magneto-Optical Study. *Photon. Res.* **2020**, *8*, A50–A55.

(17) Hayashi, T.; Kobayashi, T.; Iwanaga, M.; Watanabe, M. Exciton Dynamics Related with Phase Transitions in $CsPbCl_3$ Single Crystals. *J. Lumin.* **2001**, *95*, 255-259.

(18) Protesescu, L.; Yakunin, S.; Bodnarchuk, M. I.; Krieg, F.; Caputo, R.; Hendon, C. H.; Yang, R. X.; Walsh, A.; Kovalenko, M. V. Nanocrystals of Cesium Lead Halide Perovskites ($CsPbX_3$, X = Cl, Br, and I): Novel Optoelectronic Materials Showing Bright Emission with Wide Color Gamut. Nano Lett. **2015**, *15*, 3692-3696.

(19) Parobek, D.; Roman, B. J.; Dong, Y.; Jin, H.; Lee, E.; Sheldon, M.; Son, D. H. Exciton-to-Dopant Energy Transfer in Mn-Doped Cesium Lead Halide Perovskite Nanocrystals. *Nano Lett.* **2016**, *16*, 7376−7380.

(20) Liu, W.; Lin, Q.; Li, H.; Wu, K.; Robel, I.; Pietryga, J. M.; Klimov, V.I. Mn^{2+}-Doped Lead Halide Perovskite Nanocrystals with Dual-Color Emission Controlled by Halide Content. *J. Am. Chem. Soc.* **2016**, *138*, 14954–14961.

(21) Pan, G.; Bai, X.; Yang, D.; Chen, X.; Jing, P.; Qu, S.; Zhang, L.; Zhou, D.; Zhu, J.; Xu, W.; Dong B.; Song, H. Doping Lanthanide into Perovskite Nanocrystals: Highly Improved and Expanded Optical Properties. *Nano Lett.* **2017**, *17*, 8005-8011.

(22) Xu, K.; Vliem, J. F.; Meijerink, A. Long-Lived Dark Exciton Emission in Mn-Doped $CsPbCl_3$ Perovskite Nanocrystals. *J. Phys. Chem. C* **2019**, *123*, 979-984.

(23) Wang, Q.; Zhang, X.; Jin, Z.; Zhang, J.; Gao, Z.; Li, Y.; Liu, S. F. Energy-Down-Shift $CsPbCl_3$: Mn Quantum Dots for Boosting the Efficiency and Stability of Perovskite Solar Cells. *ACS Energy Lett.* **2017**, *2*, 1479-1486.

(24) Sun, R.; Lu, P.; Zhou, D.; Xu, W.; Ding, N.; Shao, H.; Zhang, Y.; Li, D.; Wang, N.; Zhuang, X.; Dong, B.; Bai, X.; Song, H. Samarium-Doped Metal Halide Perovskite Nanocrystals for Single-Component Electroluminescent white Light-Emitting Diodes. *ACS Energy Lett.* **2020**, *5*, 2131-2139.

(25) Zhang, X.; Zhang, Y.; Yin, W.; Wang, Y.; Wang, H.; Lu, M.; Li, Z.; Gu, Z.; Yu, W. W. Yb^{3+} and Yb^{3+}/Er^{3+} Doping for Near-Infrared Emission and Improved Stability of $CsPbCl_3$ Nanocrystals. *J. Mater. Chem. C* **2018**, *6*, 10101-10105.

(26) Su, R.; Diederichs, C.; Wang, J.; Liew, T. C. H.; Zhao, J.; Liu, S.; Xu, W.; Chen, Z.; Xiong, Q. Room-Temperature Polariton Lasing in All-Inorganic Perovskite Nanoplatelets. *Nano Lett.* **2017**, *17*, 3982-3988.

(27) Pikus, G. E.; Bir, G. L. Exchange Interaction in Excitons in Semiconductors. Zh. Eksp. Teor. Fiz. **1971**, *60*, 195−208; *Sov. Phys. JETP* **1973**, *33*, 108−114.

(28) Bir, G. L.; Pikus, G. E. Symmetry and Strain Induced Effects in Semiconductors; Wiley: New York, 1975.

(29) Denisov, M. M.; Makarov, V. P. Longitudinal and Transverse Excitons in Semiconductors.

Phys. Status Solidi B **1973**, *56*, 9-59.

(30) Manser, J. S.; Christians, J. A.; Kamat, P.V. Intriguing Optoelectronic Properties of Metal Halide Perovskites. *Chem. Rev.* **2016**, *116*, 12956-13008.

(31) Ben Aich, R.; Ben Radhia, S.; Boujdaria, K.; Chamarro, M.; Testelin, C. Multiband k·p Model for Tetragonal Crystals: Application to Hybrid Halide Perovskite Nanocrystals. *J. Phys. Chem. Lett.* **2020**, *11*, 808-817.

(32) M. Baranowski, M.; Galkowski, K.; Surrente, A.; Urban, J.; Klopotowski, L.; Machowski, S.; Maude, D. K.; Ben Aich, R.; Boujdaria, K.; Chamarro, M.; Testelin, C.; Nayak, P. K.; Dollmann, M.; Snaith, H.J.; Nicholas, R.J.; Plochocka, P. Giant Fine Structure Splitting of the Bright Exciton in a Bulk $MAPbBr_3$ Single Crystal. *Nano Lett.* **2019**, *19*, 7054-7061.

(33) Calcott, P. D. J.; Nash, K. J.; Canham, L. T.; Kane, M. J.; Brumhead, D. Identification of Radiative Transitions in Highly Porous Silicon. *J. Phys.: Condens. Matter* **1993**, *5*, L91-L98.

(34) Nirmal, M.; Norris, D. J.; Kuno, M.; Bawendi, M. G.; Efros, Al. L.; Rosen, M. Observation of the "Dark Exciton" in CdSe Quantum Dots. *Phys. Rev. Lett.* **1995**, *75*, 3728-3731.

(35) Chamarro, M.; Gourdon, C.; Lavallard, P.; Lublinskaya, O.; Ekimov, A. I. Enhancement of Electron-Hole Exchange Interaction in CdSe Nanocrystals: A Quantum Confinement Effect. *Phys. Rev. B: Condens. Matter Mater. Phys.* **1996**, *53*, 1336-1342.

(36) Micic, O. I.; Cheong, H. M.; Fu, H.; Zunger, A.; Sprague, J. R.; Mascarenhas, A.; Nozik, A. J. Size-Dependent Spectroscopy of InP Quantum Dots. *J. Phys. Chem. B* **1997**, *101*, 4904-4912.

(37) Banin, U.; Lee, J. C.; Guzelian, A. A.; Kadavanich, A. V.; Alivisatos, A. P. Exchange Interaction in InAs Nanocrystal Quantum Dots. *Superlattices Microstruct.* **1997**, *22*, 559-568.

(38) Takagahara, T. Effects of Dielectric Confinement and Electron-Hole Exchange Interaction on Excitonic States in Semiconductor Quantum Dots. *Phys. Rev. B: Condens. Matter Mater. Phys.* **1993**, *47*, 4569–4584.

(39) Rajadell, F.; Climente, J. I.; Planelles, J. Exciton in Core-Only, Core-Shell and Core-Crown CdSe Nanoplatelets: Interplay Between in-Plane Electron-Hole Correlation, Spatial Confinement and Dielectric Confinement. *Phys. Rev. B: Condens. Matter Mater. Phys.* **2017**, *96*, 035307.

(40) Benchamekh, R.; Gippius, N. A.; Even, J.; Nestoklon, M. O.; Jancu, J.-M.; Ithurria, S.; Dubertret, B.; Efros, A. L.; Voisin, P. Tight-Binding Calculations of Image-Charge Effects in Colloidal Nanoscale Platelet of CdSe. *Phys. Rev. B: Condens. Matter Mater. Phys.* **2014**, *89*, 035307.

(41) Sapori, D.; Kepenekian, M.; Pedesseau, L.; Katan, C.; Even, J. Quantum Confinement and Dielectric Profiles of Colloidal Nanoplatelets of Halide Inorganic and Hybrid Organic–Inorganic Perovskites. *Nanoscale* **2016**, *8*, 6369–6378.

(42) Ghribi, A.; Ben Aich, R.; Boujdaria, K.; Barisien, T.; Legrand, L.; Chamarro, M.; Testelin, C. Dielectric Confinement and Exciton Fine Structure in Lead Halide Perovskite Nanoplatelets. *Nanomaterials* **2021**, *11*, 3054.

(43) Fu, M.; Tamarat, P.; Trebbia, J.-B.; Bodnarchuk, M. I.; Kovalenko, M. V.; Even, J.; Lounis, B. Unraveling Exciton-Phonon Coupling in Individual $FAPbI_3$ Nanocrystals Emitting Near-Infrared Single Photons. *Nat. Commun.* **2018**, *9*, 3318.

(44) Pfingsten, O.; Klein, J.; Protesescu, L.; Bodnarchuk, M. I.; Kovalenko, M. V.; Bacher, G. Phonon Interaction and Phase Transition in Single Formamidinium Lead Bromide Quantum Dots. *Nano Lett.* **2018**, *18*, 4440–4446.

(45) Tamarat, P.; Bodnarchuk, M. I.; Trebbia, J.-B.; Erni, R.; Kovalenko, M. V.; Even, J.; Lounis, B. The Ground Exciton State of Formamidinium Lead Bromide Perovskite Nanocrystals is a Singlet Dark State. *Nat. Mater.* **2019**, *18*, 717-724.

(46) Liu, L.; Pevere, F.; Zhang, F.; Zhong, H.; Sychugov, I. Cation Effect on Excitons in Perovskite Nanocrystals from Single-Dot Photoluminescence of $CH_3NH_3PbI_3$. *Phys. Rev. B:*

Condens. Matter Mater. Phys. **2019**, *100*, 195430.

(47) Liu, L.; Zhao, R.; Xiao, C.; Zhang, F.; Pevere, F.; Shi, K.; Huang, H.; Zhong, H.; Sychugov, I. Size–Dependent Phase Transition in Perovskite Nanocrystals. *J. Phys. Chem. Lett.* **2019**, *10*, 5451-5457.

(48) Yin, C.; Chen, L.; Song, N.; Lv, Y.; Hu, F.; Sun, C.; Yu, W. W.; Zhang, C.; Wang, X.; Zhang, Y.; Xiao, M. Bright-Exciton Fine-Structure Splittings in Single Perovskite Nanocrystals. *Phys. Rev. Lett.* **2017**, *119*, 026401.

(49) Tamarat, P.; Hou, L.; Trebbia, J.-B.; Swarnkar, A.; Biadala, L.; Louyer, Y.; Bodnarchuk, M. I.; Kovalenko, M.V.; Even, J.; Lounis, B. The Dark Exciton Ground State Promotes Photon-Pair Emission in Individual Perovskite Nanocrystals. *Nat. Commun.* **2020**, *11*, 6001.

(50) Isarov, M.; Tan, L. Z.; Bodnarchuk, M. I.; Kovalenko, M. V.; Rappe, A. M.; Lifshitz, E. Rashba Effect in a Single Colloidal $CsPbBr_3$ Perovskite Nanocrystal Detected by Magneto-Optical Measurements. *Nano Lett.* **2017**, *17*, 5020-5026.

(51) Fu, M.; Tamarat, P.; Huang, H.; Even, J.; Rogach, A. L.; Lounis, B. Neutral and Charged Exciton Fine Structure in Single Lead Halide Perovskite Nanocrystals Revealed by Magneto-Optical Spectroscopy. *Nano Lett.* **2017**, *17*, 2895-2901.

(52) Ramade, J.; Andriambariarijaona, L. M.; Steinmetz, V.; Goubet, N.; Legrand, L.; Barisien, T.; Bernardot, F.; Testelin, C.; Lhuillier, E.; Bramati, A.; Chamarro, M. Fine Structure of Excitons and Electron-Hole Exchange Energy in Polymorphic $CsPbBr_3$ Single Nanocrystals. *Nanoscale* **2018**, *10*, 6393-6401.

(53) Ramade, J.; Andriambariarijaona, L. M.; Steinmetz, V.; Goubet, N.; Legrand, L.; Barisien, T.; Bernardot, F.; Testelin, C.; Lhuillier, E.; Bramati, A.; Chamarro, M. Exciton-Phonon Coupling in a $CsPbBr_3$ Single Nanocrystal. *Appl. Phys. Lett.* **2018**, *112*, 072104.

(54) Rainò, G.; Nedelcu, G.; Protesescu, L.; Bodnarchuk, M.I.; Kovalenko, M. V.; Mahrt, R. F.; Stöferle, T. Single Cesium Lead Halide Perovskite Nanocrystals at Low Temperature: Fast Single-Photon Emission, Reduced Blinking, and Exciton Fine Structure. *ACS Nano* **2016**, *10*, 2485-2490.

(55) Becker, M. A.; Vaxenburg, R.; Nedelcu, G.; Sercel, P. C.; Shabaev, A.; Mehl, M. J.; Michopoulos, J. G.; Lambrakos, S. G.; Bernstein, N.; Lyons, J. L.; Stöferle, T.; Mahrt, R. F.; Kovalenko, M. V.; Norris, D. J.; Rainò G.; Efros A. L. Bright Triplet Excitons in Caesium Lead Halide Perovskites. *Nature* **2018**, *553*, 189-193.

(56) Sercel, P. C.; Lyons, J. L.; Wickramaratne, D.; Vaxenburg, R.; Bernstein, N.; Efros, A. L. Exciton Fine Structure in Perovskite Nanocrystals. *Nano. Lett.* **2019**, *19*, 4068-4077.

(57) Heidrich, K.; Ktinzel, H.; Treusch, J. Optical Properties and Electronic Structure of $CsPbCl_3$ and $CsPbBr_3$. *Solid State Commun.* **1978**, *25*, 887-889.

(58) Peters, J.A.; Liu, Z.; De Siena, M. C.; Kanatzidis, M. G.; Wessels, B. W. Photoluminescence Spectroscopy of Excitonic Emission in $CsPbCl_3$ Perovskite Single Crystals. *J. Lumin.* **2022**, *243*, 118661.

(59) Huang, L.; Lambrecht, W. R. L. Electronic Band Structure, Phonons, and Exciton Binding Energies of Halide Perovskites $CsSnCl_3$, $CsSnBr_3$, and $CsSnI_3$. *Phys. Rev. B: Condens. Matter Mater. Phys.* **2013**, *88*, 165203.

(60) Brennan, M. C.; Forde, A.; Zhukovskyi, M.; Baublis, A. J.; Morozov, Y. V.; Zhang S.; Zhang, Z.; Kilin, D. S.; Kuno, M. Universal Size-Dependent Stokes Shifts in Lead Halide Perovskite Nanocrystals. *J. Phys. Chem. Lett.* **2020**, *11*, 4937−4944.

(61) Calistru, D. M.; Mihut, L.; Lefrant, S.; Baltog, I. Identification of the Symmetry of Phonon Modes in $CsPbCl_3$ in Phase IV by Raman and Resonance-Raman Scattering. *J. Appl. Phys.* **1997**, *82*, 5391-5395.

(62) Liao, M.; Shan, B.; Li, M. In Situ Raman Spectroscopic Studies of Thermal Stability of All-Inorganic Cesium Lead Halide ($CsPbX_3$, X = Cl, Br, I) Perovskite Nanocrystals. *J. Phys. Chem. Lett.* **2019**, *10*, 1217-1225.

(63) Guilloux, V.; Barisien, T.; Bernardot, F.; Bernard, M.; Margaillan, F.; Majrab, S.; Stenger, I.; Lhuillier, E.; Testelin, C.; Chamarro, M.; Legrand, L. Phonon Modes and Exciton-Phonon Interactions in $CsPbCl_3$ Single Nanocrystals. *Physica E* **2023**, *151*, 115713.

(64) Weinberg, D.; Park, Y.; Limmer, D. T.; Rabani E. Size-Dependent Lattice Symmetry Breaking Determines the Exciton Fine Structure of Perovskite Nanocrystals. doi.org/10.1021/acs.nanolett.3c00861.

(65) Bertolotti, F.; Protesescu, L.; Kovalenko, M. V.; Yakunin, S.; Cervellino, A.; Billinge, S. J. L.; Terban, M. W.; Pedersen, J. S.; Masciocchi, N.; Guagliardi, A. Coherent Nanotwins and Dynamic Disorder in Cesium Lead Halide Perovskite Nanocrystals. *ACS Nano* **2017**, *11*, 3819–3831.

(66) Sercel, P. C.; Lyons, J. L.; Bernstein, N.; Efros, A. L. Quasicubic Model for Metal Halide Perovskite Nanocrystals. *J. Chem. Phys*. **2019,** *151*, 234106.

(67) Ghribi, A.; Ben Radhia, S.; Boujdaria, K.; Legrand, L.; Barisien, T.; Chamarro, M.; Testelin, C. Dielectric Effects, Crystal Field, and Shape Anisotropy Tuning of the Exciton Fine Structure of Halide Perovskite Nanocrystals. *Phys. Rev. Materials* **2022**, *6*, 106001.

(68) Ben Aich, R.; Saïdi, I.; Ben Radhia, S.; Boujdaria, K.; Barisien, T.; Legrand, L.; Bernardot, F.; Chamarro, M.; Testelin, C. Bright-Exciton Splittings in Inorganic Cesium Lead Halide Perovskite Nanocrystals. *Phys. Rev. Applied* **2019**, *11*, 034042.

(69) Han, Y.; Liang, W.; Lin, X.; Li, Y.; Sun, F.; Zhang, F.; Sercel, P.C.; Wu, K. Lattice Distortion Inducing Exciton Splitting and Coherent Quantum Beating in $CsPbI_3$ Perovskite Quantum Dots. *Nat. Mater.* **2022**, *21*, 1282–1289.

(70) Kopteva, N. E.; Yakovlev, D. R.; Kirstein, E.; Zhukov, A.; Kudlacik, D.; Kalitukha, I. V.; Sapega, V. F.; Dirin, D. N.; Kovalenko, M. V.; Baumann, A.; Höcker, J.; Dyakonov, V.; Crooker, S.A.; Bayer, M. Weak Dispersion of Exciton Landé Factor with Band Gap Energy in Lead Halide Perovskites: Approximate Compensation of the Electron and Hole Dependences. *arXiv:2301.12775v1*.

(71) Tsitsishvili, E.; Baltz, R.V.; Kalt, H. Temperature Dependence of Polarization Relaxation in Semiconductor Quantum Dots. *Phys. Rev. B: Condens. Matter Mater. Phys.* **2002**, *66*, 161405(R).

(72) Diroll, B. T.; Zhou, H.; Schaller, R. D. Low-Temperature Absorption, Photoluminescence, and Lifetime of $CsPbX_3$ (X = Cl, Br, I) Nanocrystals. *Adv. Funct. Mater.* **2018**, *28*, 1800945.

(73) Rossi, D.; Qiao, T.; Liu, X.; Khurana, M.; Akimov, A. V.; Cheon, J.; Son, D. H. Size-Dependent Dark Exciton Properties in Cesium Lead Halide Perovskite Quantum Dots. *J. Chem. Phys.* **2020**, *153*, 184703.